International Symposium
On Turbulence and Shear Flow
Phenomena (TSFP-8)
August 28 - 30, 2013 Poitiers, France

INVESTIGATION OF WALL-BOUNDED TURBULENCE OVER REGULARLY DISTRIBUTED ROUGHNESS

Marco Placidi
Faculty of Engineering and the Environment
Aerodynamics and Flight Mechanics Group
University of Southampton
Highfield, Southampton, SO17 1BJ, UK
m.placidi@soton.ac.uk

Bharathram Ganapathisubramani
Faculty of Engineering and the Environment
Aerodynamics and Flight Mechanics Group
University of Southampton
Highfield, Southampton, SO17 1BJ, UK
g.bharath@soton.ac.uk

ABSTRACT

Experiments were conducted in the fully-rough regime on surfaces consisting of regularly distributed Lego bricks of uniform height, arranged in different configurations. Measurements were made with high resolution planar Particle Image Velocimetry on six different configurations at different frontal solidity, λ_F, and fixed plan solidity, λ_P.

Results indicate that mean velocity profiles in defect form conforms to outer-layer similarity. However, streamwise, wall-normal turbulent intensities and particularly Reynolds shear stresses show a lack of similarity across the different cases. Quadrant analysis reveals an increase in Q_4 and in Q_2 activities in the outer layer which is dependent on the frontal solidity. Proper Orthogonal Decomposition show an increase in fractional and cumulative turbulent kinetic energy contribution of the lowest-order modes with increasing the density of the elements, indicating a redistribution of the energy toward the larger-scales.

INTRODUCTION

Surface roughness is found in abundance in natural environments and plays an important role in a variety of practical and engineering applications. Nevertheless, while rough-walls are of great importance, they are much less understood than their smooth-wall counterpart (Jimenez, 2004). It has been known since Hama (1954) and Clauser (1956) that the influence of roughness on the law of the wall is mainly a downward shift in the logarithmic portion of the smooth-wall curve. For a rough-wall boundary layer, the velocity profile in the log-region can, in fact, be express as:

$$U^+ = \frac{1}{\kappa}\ln\left(\frac{y-d}{y_0}\right) \equiv \frac{1}{\kappa}\ln(y-d)^+ + B - \Delta U^+, \quad (1)$$

where κ is the von Kármán constant ($\kappa \approx 0.36-0.44$ Segalini *et al.* (2013)) and B is the smooth-wall intercept. The downward shift is represented by the roughness length y_0, or equivalently by ΔU^+ and d is the zero-plane displacement. Since Schlichting (1979), the tendency has been to characterise the effect of regularly distributed roughness using two density parameters: frontal and plan solidities. The frontal solidity, λ_F, is defined as the total projected frontal area of the roughness elements per unit wall-parallel area; while the plan solidity, λ_P, is the ratio between the plan area and the unit wall-parallel area. Various studies have examined the effect of surface morphology on the bulk drag, and attempted to find correlations for $y_0 = f(\lambda_F, \lambda_P)$. These studies demonstrated that the flow is characterised by two regimes: sparse ($\lambda_F < 0.15$), in which y_0 increases with solidity, and dense ($\lambda_F \geq 0.15$), for which y_0 decreases due to the roughness elements sheltering each other (Jimenez, 2004). Although the trend of the roughness length variation with frontal solidity seems to be well established, a review of numerous studies by Grimmond & Oke (1998) only suggested a theoretical peak in y_0 for $\lambda_p \approx 0.35$. Nevertheless, this is inconsistent with some other studies, such as Leonardi & Castro (2010), who reported this peak to be at $\lambda_p \approx 0.15$ for cubical arrays. Reviews of different predicting algorithms for y_0 and an analysis of their accuracy can be found in Grimmond & Oke (1998), Macdonald (2000) and more recently in Millward-Hopkins *et al.* (2011).

Another important aspect of rough-wall boundary layers is the validity of Townsend's similarity hypothesis. Raupach *et al.* (1991) performed an extensive literature review and found strong evidence for outer-layer similarity in the structure of turbulence in between smooth and rough-walls. This theory has been more recently supported by Jimenez (2004) who also pointed out that the behaviour of the mean statistics depends on the severity of the surface protrusion. Amir & Castro (2011), amongst others, also supported this

argument and suggested that outer-layer similarity holds for surface protrusions that extend up to 15% of the boundary layer thickness. Nevertheless, evidence of a lack of similarity has been found by Krogstad & Antonia (1999) and lately by Volino *et al.* (2009) for 2D roughness element and by Ganapathisubramani & Schultz (2011) for a sparse distribution of regular roughness.

In this study, the aim is to examine the effects of frontal solidity on the roughness length (i.e. the bulk drag), the structure of the turbulence/momentum transfer and the validity of Townsend's similarity hypothesis.

EXPERIMENTAL FACILITY AND DETAILS

The present experiments were carried out in a suction wind tunnel at the University of Southampton. The tunnel has a working section of 4.5 m in length, with a 0.9 $m \times 0.6$ m cross section. The free-stream turbulence intensity in the tunnel has been verified through hot wire anemometry measurements, to be homogenous along the spanwise and wall-normal directions and less than 0.5%. In this study, the streamwise, wall-normal and spanwise directions are given along the $x-y-z$ directions and $u-v-w$ are the corresponding velocities. Fluctuating velocities are denoted with a $'$, while the letters are capitalised to represent the mean. The free-stream velocity in the wind tunnel was measured by a Pitot-static tube and all the measurements were carried out at a velocity of 11.5 m/s. Experiments were conducted in nominally zero-pressure-gradient (ZPG) as $\frac{\nu}{\rho U_\tau}\frac{dP}{dx} < 4.5\times10^{-5}$. For rough surfaces, this study used a LEGO baseboard onto which rectangular LEGO bricks (or blocks), uniformly distributed in staggered array, were securely fixed. These bricks presented a uniform height ($h =$ 11.4 mm). Six different patterns were adopted in order to systematically examine the individual effects of frontal solidity on the structure of the turbulence. The different cases were designed on the basis of Grimmond & Oke (1998) and Jimenez (2004) predictions for the peak in $y_0 = f(\lambda_F, \lambda_P)$. More specifically, the plan solidity was kept constant whilst varying the frontal solidity as shown in Table 1. Figures 1(a) & (b) show the geometry of a LEGO element and the basic repetitive units adopted to generate the different patterns in analysis. Progressive repositioning of the roughness elements in the sheltered regions of the upstream obstacles, has allowed to achieve variations in frontal solidity at fixed plan solidity. The unit wall-parallel area of each repetitive units was also fixed at 70.2 $mm \times 39$ mm. Analogous cases for λ_P variations at fixed λ_F were also investigated although not presented in this paper. In evaluating λ_F and λ_P, the complete LEGO bricks has been considered (including the pins on top of the blocks). A fetch length of about 20 times the boundary-layer thickness, δ, was covered with brick elements. Such a long fetch is necessary in order to guarantee the fully rough regime (Castro, 2007). Measurements were taken at approximately 4 m downstream in the elements' field. Flow measurements were acquired using planar Particle Image Velocimetry (PIV). The flow was seeded with vaporised glycol-water solution particles (1 μm in diameter) illuminated with a 1 mm thick laser sheet produced by a pulsed New Wave Nd:YAG laser System operating at 200 mJ. Streamwise wall-normal (x,y) planes were acquired at the spanwise centreline of the test section by a 16 M *pixel* high resolution LaVision camera equipped with Nikon 105 mm f/8 lenses. For each run, sets of 2000 pairs of digital images were captured and processed with *DaVis 8.0*

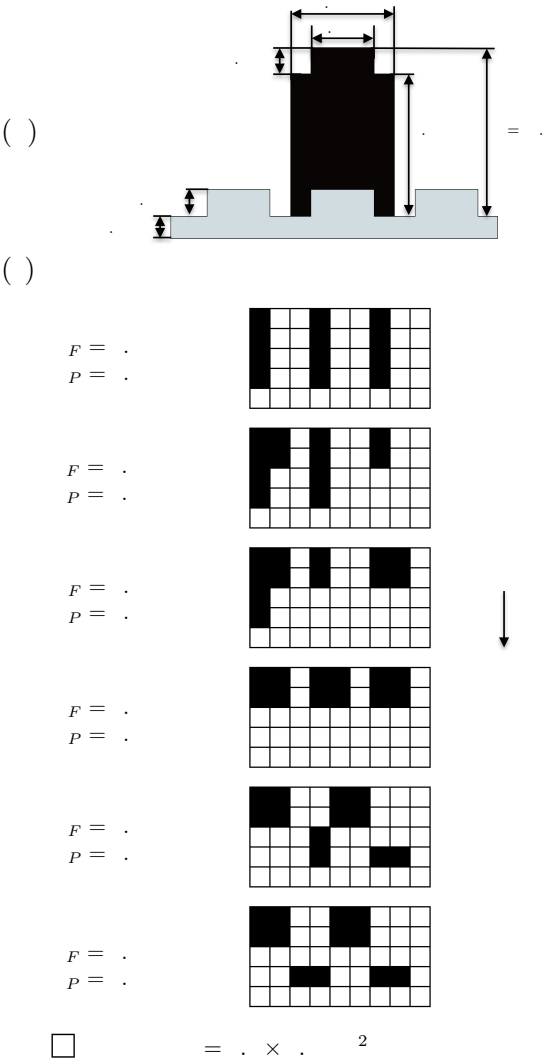

Figure 1. (a) LEGO brick geometry and (b) Roughness elements' patterns with varying λ_F at $\lambda_P = const = 0.27$.

software. This apparatus allowed a field of view of approximately $1.8\delta \times 1.3\delta$ (streamwise-spanwise) to be resolved. Velocity vectors were obtained using 16×16 pixel interrogation windows with 50% overlap. The resulting spatial resolution is approximately 0.7 $mm \times 0.7$ mm (l^+ ranging in between 30 and 40) and successive vectors are spaced at half that distance (due to 50% overlap). Stereoscopic PIV vector fields were also acquired at two different wall-normal locations: at the top of the canopy and outside the roughness sublayer. These results are not presented here but were used to confirm the spanwise homogeneity, at least in the outer region.

The skin friction velocity, $U_\tau = \sqrt{\tau_{wall}/\rho}$, where τ_{wall} is the wall total shear stress and ρ is the density of the fluid, is normally assumed to be the average shear stress in the log-region. However Cheng & Castro (2002) argued that, for boundary-layer flows over staggered arrays of cubical elements, the $\rho\overline{u'v'}$ underestimates the surface stress by some 24%. Therefore, in this study, we use a corrected estimate, defined as (Castro & Reynolds, 2008):

$$U_\tau = 1.12\sqrt{-\overline{u'v'}}\Big|_{2<y/h<3}; \qquad (2)$$

Table 1. Relevant experimental parameters.

Dataset	λ_F	λ_P	$\delta(mm)$	h/δ	$U_\tau(m/s)$	Re_τ	$\delta^*(mm)$	h^+	d/h	y_0/h	$y_0{}^+$
LF1	0.09	0.27	110.9	0.102	0.6013	4636	16.8	470	0.90	0.0168	7.9
LF2	0.12	0.27	122.0	0.090	0.6654	5640	22.0	519	0.92	0.0258	13.5
LF3	0.15	0.27	121.1	0.093	0.6653	5861	22.3	545	0.83	0.0385	20.9
LF4	0.18	0.27	122.1	0.093	0.7591	6443	24.4	593	0.74	0.0828	40.1
LF5	0.21	0.27	129.2	0.088	0.8152	7351	26.9	635	0.60	0.1160	73.7
LF6	0.24	0.27	126.7	0.090	0.8098	7147	26.5	630	0.70	0.1069	67.5

where the Reynolds shear stress included in the calculation come from the plateau region in the roughness sublayer (as in Flack *et al.* (2005) and Castro (2007)). The U_τ value from this approach is within 5% of the value obtained by assuming the skin friction to be the maximum of the Reynolds shear stresses as in Manes *et al.* (2011). Once the skin friction velocity was calculated, a least square fit procedure was adopted to evaluate firstly the zero-plane displacement, d and then the roughness length, y_0. This method assumes that a log-layer exists for data from $y \geq 1.5h$ and $y/\delta \leq 0.2$. The fitting procedure was carried out with $\kappa = 0.38$. An additional procedure, based on a modified indicator function, was also applied for comparison. In the latter, the zero-plane displacement is evaluated by minimising the slope of the indicator function, Ξ, as in Nagib & Chauhan (2008). This function should, in fact, be a constant in the log-region. The roughness length is then determined simply minimising the residual. The discrepancy of the values across different cases obtained using the two methods was, on average, approximately 25% for the zero-plane displacement and 17% for y_0. This is within the range reported in the literature given the uncertainty in determination of the skin-friction velocity (Acharya *et al.*, 1986), the log-law boundaries Segalini *et al.* (2013) and the value of the von Kármán constant (Castro (2007) and Segalini *et al.* (2013). The calculated aerodynamic parameters and some relevant boundary-layer characteristics are given in Table 1.

RESULTS

Effect of surface morphology on the bulk drag

Figure 2 shows the mean velocity profiles in inner scale for the different cases of λ_F. It can be seen that, compared to a smooth-wall case (Eq. 1 with $d = 0$, $B = 5$ and $\Delta U^+ = 0$), the roughness is responsible for a uniform downward shift in the log-region. This downward shift (i.e. y_0/h) increases, as the elements' density, λ_F, increases. The plain baseboard case, referring to the wind tunnel floor being covered only with LEGO baseboard but no bricks, is also reported for comparison. It can be seen that the presence of the Lego blocks (case LF1 to LF6) is indeed responsible for generating most of the bulk drag, rather than the protrusion that characterises the baseboard itself. These results (i.e. y_0/h in Table 1) are qualitatively consistent with the $y_0/h = f(\lambda_F)$ predictions from Macdonald (2000) shown in the inset plot in Figure 2. The current data set does not seem to reveal a peak in bulk drag for $\lambda_F = 0.15$ as from Jimenez (2004), perhaps due to the fixed value of λ_P examined in the study.

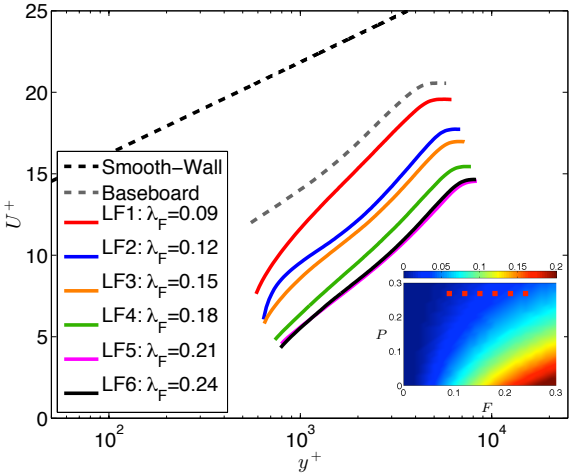

Figure 2. Mean velocity profiles in inner scales as a function of λ_F ($\lambda_P = const = 0.27$). Inset: Prediction of normalised $y_0 = f(\lambda_F, \lambda_P)$ calculated using Macdonald (2000) correlations. Colorbar shows y_0/h. Red points represent the current data set.

Mean-flow similarity

Figure 3 shows the mean velocity profiles in defect form. To normalise the wall-normal distance the Clauser's scaling parameter is here used as in Castro (2007) and Amir & Castro (2011). This parameter is defined as $\Delta = (\delta^* U_e)/U_\tau$, where δ^* is the displacement thickness, and U_e the velocity at the edge of the boundary layer. The mean velocity profiles show a good agreement across all the different cases throughout the entire outer region (i.e. $(y-d)/\Delta \geq 0.02$).

Figure 4 shows the streamwise and the wall-normal velocity fluctuations for different values of λ_F. The streamwise turbulent intensity presents a reasonable collapse of the data for $(y-d)/\Delta > 0.2$ and major differences appear closer to the wall. The LF2 and LF3 cases exhibit largest differences and departure from the other cases for $(y-d)/\Delta < 0.2$. The wall-normal turbulence intensities show a similar behaviour throughout the entire range of wall-normal locations. These findings are consistent with previous studies who found a lack of similarity for lower values of frontal solidities, especially in 2D roughness elements (Volino *et al.*, 2007).

Figure 5 presents the Reynolds shear stress for the different cases of λ_F. The Reynolds stress values seem to be affected by the solidity; this effect results in a lack of similarity throughout the entire $(y-d)/\Delta$ range. In cases of LF2 and LF3, which are presumed to be in the vicinity of a

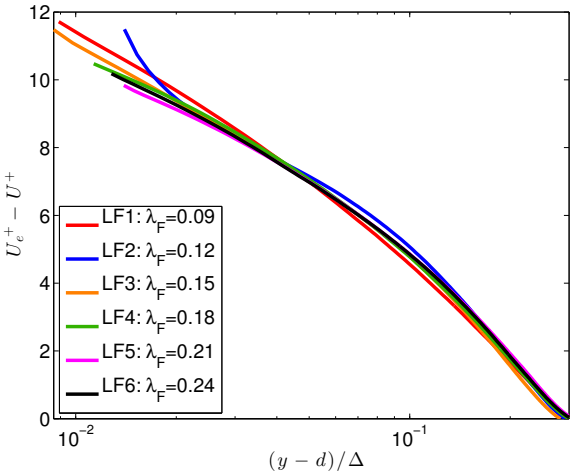

Figure 3. Mean velocity profiles in defect form as a function of λ_F ($\lambda_P = const = 0.27$).

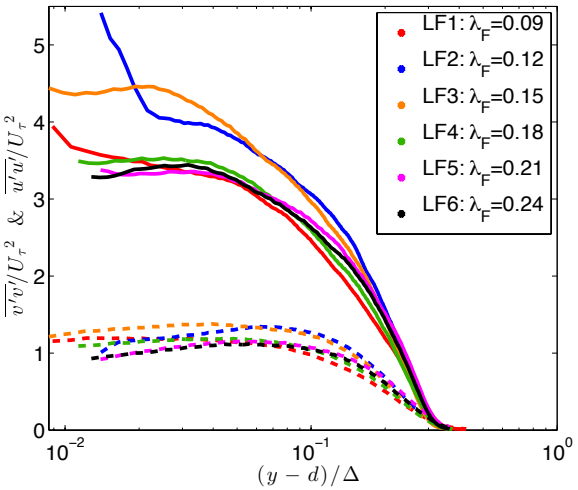

Figure 4. Wall-normal variation of streamwise turbulence intensity ($\overline{u'u'}/{U_\tau}^2$ solid lines) and wall-normal turbulence intensity ($\overline{v'v'}/{U_\tau}^2$ dashed lines) as a function of λ_F ($\lambda_P = const = 0.27$).

peak in y_0 (as from Grimmond & Oke (1998)), the Reynolds shear stresses and the turbulent fluctuations show the largest deviation with respect to the other cases. However, it must be noted that we not observe a peak in y_0 in our data as the value of y_0 just increases with increasing λ_F. This is likely due to the fact that our λ_P is not at an optimal value to observe this trend. This behaviour has to be further investigated.

Quadrant Analysis

To further investigate the behaviour of the Reynolds shear stresses, a quadrant decomposition and subsequent analysis has been carried out. This analysis is based on the hyperbolic hole size, H, following Lu & Willmarth (1973). This separates turbulent events into four quadrants in the $(u' - v')$ plane, in order to understand the significant events to the momentum transfer. The second quadrant (Q_2: $u' < 0$ & $v' > 0$) representing the ejections, and the fourth quadrant (Q_4: $u' > 0$ & $v' < 0$) representing the sweeps are the objects of this investigation. Although a range of hyperbolic holes was investigated, only results for $H = 2.5$ (corresponding to events with $u'v' > 6\overline{u'v'}$) are presented. Figures 6(a) & (b) show the percentage contribution to the total shear stress provided by strong ejection and sweep events, Q_2 and Q_4, respectively. For clarity, only cases LF1, LF3 and LF6 are shown, since the others present a behaviour following the trend highlighted by those three cases. Both the Q_2 and Q_4 show a gradual increase in activity with increasing value of the frontal solidity.

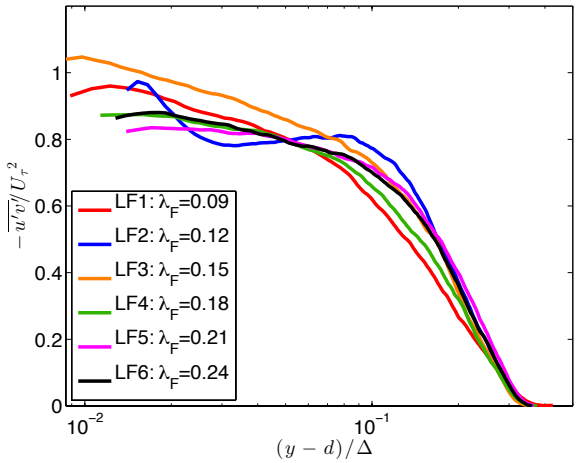

Figure 5. Wall-normal variation of Reynolds shear stress ($\overline{-u'v'}/{U_\tau}^2$) as a function of λ_F ($\lambda_P = const = 0.27$).

Figure 6(c) shows the ratio Q_2/Q_4 for the different cases across different wall-normal locations. For a rough-wall boundary layer, Q_2 events (ejections) consistently dominate on Q_4 events (sweeps) almost throughout the entire y/Δ range. However, for $y/\Delta < 0.05$, it can be seen that this ratio is less than unity for all the cases, suggesting that sweeps are important within the roughness sublayer. This is consistent with observations in previous studies (Amir & Castro, 2011). Another point to note is the wall-normal extent at which the reversal in the ratio occurs in the outer region. It can be seen in figure 6(c) that as λ_F increases, this region of reversal occurs closer to the wall. Perhaps, this can be interpreted as a decreasing impact in the wall-normal extent (in terms of momentum transfer) with increasing λ_F.

Proper Orthogonal Decomposition

To further explore the fluctuating velocity field and its energy content as a function of spatial scales, a method snapshot based proper orthogonal decomposition (POD) analysis (Berkooz *et al.*, 1993) has been carried out. This technique generates a basis for modal decomposition of ensemble of instantaneous fluctuating velocity fields, provides the most efficient way of identifying the motions which, on average, contain a majority of the turbulent kinetic energy (TKE) in the flow (Palmer *et al.*, 2011). The energy contribution of the singular value across the modes depends on the local spatial resolution of the data set as Pearson (2012) has shown. This is because the energy content of each ith mode depends on the smallest resolved scale in the flow. The global resolution of the current data set ranges in between 30 to 40 wall-units, due to differences in the skin friction velocity generated by the different surface morphologies. This results in a variation of the Kármán number in the range of $Re_\tau \approx 4600 - 8400$. For this reason, the current data set has been downsampled with a low-pass Gaus-

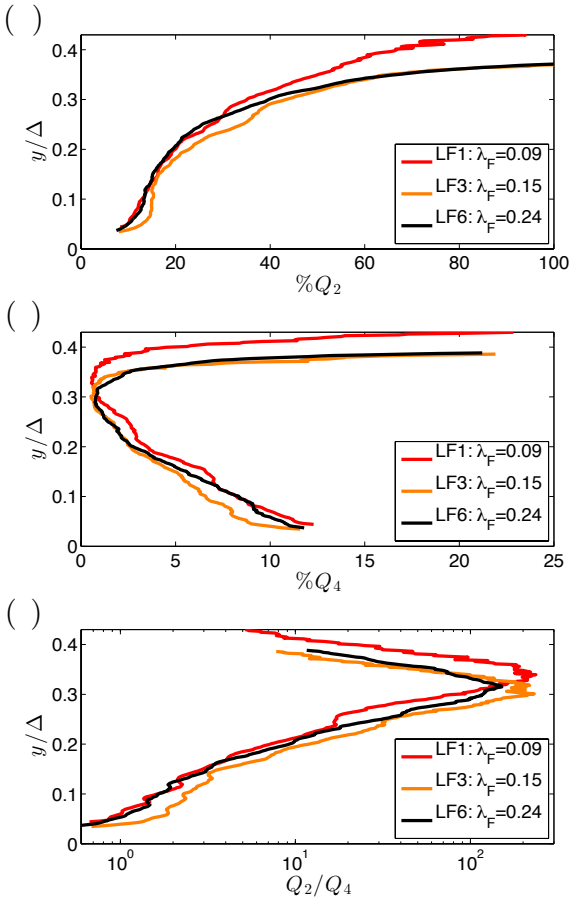

Figure 6. Percentage contributions to $\overline{u'v'}$ for $H = 2.5$ from (a) Q_2 and (b) Q_4 events as a function of λ_F ($\lambda_P = const = 0.27$). (c) Ratio of the shear stress contributions from Q_2 and Q_4 events for $H = 2.5$ as a function of λ_F ($\lambda_P = const = 0.27$).

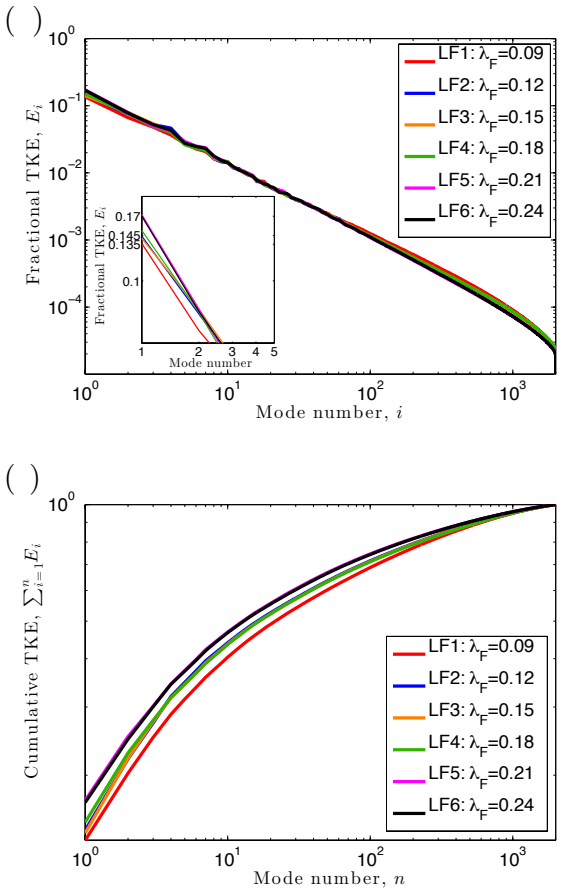

Figure 7. (a) Fraction of TKE, E_i and (b) cumulative turbulent kinetic energy content, $\sum_{i=1}^{n} E_i$ versus mode number as a function of λ_F ($\lambda_P = const = 0.27$).

sian filter designed to match the local resolution at $l^+ = 45$. Moreover, as the POD modes calculation is performed over the combined (u, v) data, the u-data contains the larger spatial modes. Instantaneous 2-D velocity fields from the top of the elements up to the boundary layer thickness are included in the POD calculation. As Liu *et al.* (2001) discussed, while POD modes are not representative of the actual coherent structures present in the flow, but more of the energy of those structures, they do provide a qualitative glimpse of the dominant flow field associated with each ith mode and its variability. Although not shown here for brevity, our analysis shows that the first four modes (low-order modes) present identical shapes across the different cases and embody progressively smaller spatial scales of the flow. From mode 5 onward, the effect of the surface morphology manifest, resulting in varying POD modes shapes depending upon the surface morphologies. However, the amount of kinetic energy within each of these first four modes are different. Figure 7(a) shows the fractional TKE contribution E_i, of the ith POD mode, ϕ_i, to the total TKE (here defined as $TKE = (u'^2 + v'^2)^{1/2}$ since the the out-of-plane velocity component is not available). It can be seen in the inset plot that cases with lower λ_F tend to be characterised by lower energy content in the first POD modes. For example, mode 1 for the LF6 case contributes to $\approx 17\%$ of the total energy, while its contribution for the LF3 and LF1 cases, is only $\approx 14\%$ and $\approx 13.5\%$ respectively. Moreover, the cumulative TKE (Figure 7(b)) of the first 4 modes contributes to $\approx 28.7\%$ of the total TKE for the sparsest case, LF1, and reaches contributions of $\approx 34.4\%$ for the densest case, LF6. This seems to suggest that the effect of an increased frontal solidity would be to redistribute the energy toward the lowest-order POD modes and therefore the larger-scales.

CONCLUSIONS

Experiments were conducted in fully-rough regime on surfaces consisting of regularly distributed Lego bricks of uniform height, arranged in staggered arrays. Measurements were made on six different cases with systematically increased frontal solidity, with high resolution planar PIV in the following Kármán number range: $Re_\tau \approx 4600 - 8400$.

The results indicate that mean velocity profiles in defect form conforms to outer-layer similarity. However, both streamwise and wall-normal turbulent intensities and Reynolds shear stresses show a lack of similarity related to changes in solidities. The differences in fluctuating velocity profiles is confirmed by an increase in Q_2 and Q_4 activities, depending upon the frontal solidity. POD analysis showed, on average, an increase in both fractional and cumulative turbulent kinetic energy contributions in the lowest-order modes when the density of the roughness elements was increased, indicating a redistribution of the energy toward the larger-scales. The current experiments do not show a

peak value in drag for $\lambda_F = 0.15$ instead show that the drag monotonically increases (within experimental uncertanty) with increasing value of λ_F.

ACKNOWLEDGEMENTS

The authors are grateful to the Lloyd's Register Foundation (LRF) for supporting this research. We also acknowledge the support from the European Research Council under the European Union's Seventh Framework Programme (FP7/2007-2013) / ERC Grant agreement No. 277472.

REFERENCES

Acharya, M, Bornstein, J & Escudier, M P 1986 Turbulent boundary layers on rough surfaces. *Experiments in Fluids* **4**, 33–47.

Amir, M & Castro, I P 2011 Turbulence in rough-wall boundary layers: universality issues. *Experiments in Fluids* **51**, 313–326.

Berkooz, G, Holmes, P & Lumley, J L 1993 The proper orthogonal decomposition in the analysis of turbulent flows. *Annual Review of Fluid Mechanics* **25**, 539–575.

Castro, I P 2007 Rough-wall boundary layers: mean flow universality. *Journal of Fluid Mechanics* **585**, 469–485.

Castro, I P & Reynolds, R T 2008 Measurements in an urban-type boundary layer. *Experiments in Fluids* **45** (1), 141–156.

Cheng, H & Castro, I P 2002 Near wall flow over urban-like roughness. *Boundary-Layer Meteorology* **104**, 229–259.

Flack, K A, Schultz, M P & Shapiro, T A 2005 Experimental support for Townsend's Reynolds number similarity hypothesis on rough walls. *Physics of Fluids* **17** (3), 035102.

Ganapathisubramani, B & Schultz, M P 2011 Turbulent boundary layer structure over sparsely distributed roughness. In *7th International Symposium on Turbulence and Shear flow phenomena, Ottawa, Canada July 28–31*.

Grimmond, C S B & Oke, T R 1998 Aerodynamic properties of urban areas derived, from analysis of surface form. *Journal of Applied Meteorology* **38** (9), 1262–1292.

Jimenez, J 2004 Turbulent flows over rough walls. *Annual Review of Fluid Mechanics* **36** (1), 173–196.

Krogstad, P A & Antonia, R A 1999 Surface roughness effects in turbulent boundary layers. *Experiments in Fluids* **27**, 450–460.

Leonardi, S & Castro, I P 2010 Channel flow over large cube roughness: a direct numerical simulation study. *Journal of Fluid Mechanics* **651**, 519–539.

Liu, Z C, Adrian, R J & Hanratty, T J 2001 Large-scale modes of turbulent channel flow: transport and structure. *Journal of Fluid Mechanics* **448**, 53–80.

Lu, S. S. & Willmarth, W. W. 1973 Measurements of the structure of the Reynolds stress in a turbulent boundary layer. *Journal of Fluid Mechanics* **60** (3), 481–511.

Macdonald, R W 2000 Modelling The Mean Velocity Profile In The Urban Canopy Layer. *Boundary-Layer Meteorology* **97**, 25–45.

Manes, C, Poggi, D & Ridolfi, L 2011 Turbulent boundary layers over permeable walls: scaling and near-wall structure. *Journal of Fluid Mechanics* **687**, 141–170.

Millward-Hopkins, J T, Tomlin, A S, Ma, L, Ingham, D & Pourkashanian, M 2011 Estimating Aerodynamic Parameters of Urban-Like Surfaces with Heterogeneous Building Heights. *Boundary-Layer Meteorology* pp. 467–490.

Nagib, H M & Chauhan, K A 2008 Variations of von Kármán coefficient in canonical flows. *Physics of Fluids* **20** (10), 101518.

Palmer, J A, Mejia-Alvarez, R, Best, J L & Christensen, K T 2011 Particle-image velocimetry measurements of flow over interacting barchan dunes. *Experiments in Fluids* **52** (3), 809–829.

Pearson, D S 2012 Characterisation and estimation of the flow over a forward-facing step. PhD thesis, Imperial College London. Department of Aeronautics.

Raupach, M R, Antonia, R A & Rajagopalan, S 1991 Rough-Wall Turbulent Boundary Layers. *Applied Mechanics Reviews* **44** (1), 1–25.

Schlichting, H 1979 *Boundary Layer Theory*. Springer.

Segalini, A, Örlü, R & Alfredsson, P H 2013 Uncertainty analysis of the von Kármán constant. *Experiments in Fluids* **54** (2), 1460.

Volino, R J, Schultz, M P & Flack, K A 2007 Turbulence structure in rough- and smooth-wall boundary layers. *Journal of Fluid Mechanics* **592**, 263–293.

Volino, R J, Schultz, M P & Flack, K A 2009 Turbulence structure in a boundary layer with two-dimensional roughness. *Journal of Fluid Mechanics* **635**, 75–101.